System-Independent Characterization of Materials Using Dual-Energy Computed Tomography

Stephen G. Azevedo, *Senior Member, IEEE*, Harry E. Martz, Jr., Maurice B. Aufderheide, III, *Member, IEEE*, William D. Brown, Kyle M. Champley, Jeffrey S. Kallman, G. Patrick Roberson, Daniel Schneberk, Isaac M. Seetho, and Jerel A. Smith, *Member, IEEE*

***Abstract*—We present a new decomposition approach for dual-energy computed tomography (DECT) called SIRZ that provides precise and accurate material description, independent of the scanner, over diagnostic energy ranges (30 to 200 keV). System independence is achieved by explicitly including a scanner-specific spectral description in the decomposition method, and a new X-ray-relevant feature space. The feature space consists of electron density, ρ_e, and a new effective atomic number, Z_e, which is based on published X-ray cross sections. Reference materials are used in conjunction with the system spectral response so that additional beam-hardening correction is not necessary. The technique is tested against other methods on DECT data of known specimens scanned by diverse spectra and systems. Uncertainties in accuracy and precision are less than 3% and 2% respectively for the (ρ_e, Z_e) results compared to prior methods that are inaccurate and imprecise (over 9%).**

***Index Terms*—Beam-hardening correction, dual-energy computed tomography, effective atomic number, electron density, photoelectric-compton decomposition, quantitative x-ray characterization, system-independent CT.**

I. Introduction

FOR decades, researchers in X-ray computed tomography (CT) for medical [1], security [2], and nondestructive characterization (NDC) applications [3] have attempted to extend the imaging function of CT into a full description of the physical and chemical makeup of an object [4]–[7]. In imaging for flaws, relative (not absolute) intensity values are often sufficient, but material and object characterization requires both accurate and precise results that are independent of the DECT spectra or system. For example, one would like to understand the elemental composition of concrete [8] or to distinguish explosive from benign materials in luggage [9]. An ideal type of characterization would include high-resolution estimates of both mass density (ρ) and atomic number (Z) of all constituent elements and compounds in each volume element (voxel).

Instead, single-energy CT measures voxelized X-ray linear attenuation coefficients (μ) that depend on scanner-based factors, mainly the system spectral response, so that a single CT image cannot produce accurate estimates of ρ and Z. Spectral differences between scans can be due to a variety of issues such as source or detector energy shifts caused by aging, detector nonlinearities, X-ray scatter and blur, filtration materials, direct conversion, absorption edges, calibration errors, electronic noise, and other anomalies. Additionally, these X-ray spectral changes are difficult to measure, calibrate and rectify.

Dual-energy computed tomography (DECT) has emerged as a better way to estimate density and effective atomic number, or Z_{eff} as defined in [10], by scanning an object with two different X-ray spectral ranges [1], [2], [11]–[24]. Depending on the spectra used, the low- (μ_{low}) and high-energy (μ_{high}) attenuation coefficients from a DECT scan provide crude small-volume (μm^3 to mm^3) estimates of electron density (ρ_e) and Z_{eff}, which are roughly proportional to μ_{high} and the ratio of μ_{low} to μ_{high}, respectively. Still, while μ_{low} and μ_{high} values may be precise and repeatable on a well-calibrated system, these features suffer from the same CT energy-spectrum dependence leading to inaccuracies in the estimates of compositional makeup. Typical DECT results are weakly correlated to the material ρ and Z, and they can vary as the spectral responses change between systems or over time.

This paper studies the extent to which existing and new ways of processing DECT data for metrology of physical material properties can produce system-independent results. ("System" or "scanner" are used interchangeably here, though spectrum independence is the main goal.) That is, we are exploring how closely (accuracy) and repeatably (precision) the DECT results match those properties regardless of scanner or spectrum used to near the uncertainty level of the X-ray measurements themselves (a few percent). To that end, we introduce in Section II an alternate feature space, or basis set, which is based on known X-ray properties of materials in the energy range of most medical, NDC and checked-baggage DECT scanners. A corresponding DECT processing method called SIRZ is presented in Section III and it is described relative to prior art that uses other feature spaces. Like other methods, SIRZ employs scans of carefully-chosen reference materials to estimate and correct for the system spectral response. To assess the system- and/or spectral-independence of the results, Section IV describes a set of experiments performed using multiple pairs of energy ranges on two separate DECT systems. Results and comparative analyses of measuring material properties with these methods are presented in Section V, including accuracy, precision, and sensitivity to spectral model mismatches. Sections VI and VII present a discussion of the results and future research areas followed by concluding remarks.

Manuscript received March 28, 2015; revised July 22, 2015; accepted December 27, 2015. Date of current version February 16, 2016. This research was funded by the Science & Technology Directorate of the Department of Homeland Security (DHS). This work was performed under the auspices of the U.S. Department of Energy by Lawrence Livermore National Laboratory under Contract DE-AC52-07NA27344. LLNL Document number LLNL-JRNL-678559.

The authors are with the Lawrence Livermore National Laboratory, Livermore, CA 94551, USA (e-mail: steve.azevedo@gmail.com).

Digital Object Identifier 10.1109/TNS.2016.2514364

0018-9499 © 2016 IEEE. Translations and content mining are permitted for academic research only. Personal use is also permitted, but republication/redistribution requires IEEE permission. See http://www.ieee.org/publications_standards/publications/rights/index.html for more information.

II. X-RAY FEATURE SPACES

In this section we describe common X-ray features that can be used as basis variables for DECT processing.

A. Conventional DECT Feature Space—(μ_{high}, μ_{low}/μ_{high})

The simplest and most common way to process DECT values of μ_{low} and μ_{high} into material properties is to recognize that the higher-energy contributions to X-ray attenuation for common spectra up to 200 keV and higher are dominated by Compton scatter, which causes the observed μ_{high} to trend with the density of the material. The ratio of the low- to high-energy attenuation coefficients, on the other hand, trends monotonically with the effective atomic number of the specimen to first order [1]. Then, a common way to use μ_{low} and μ_{high} values at these DECT energies is with the "Ratio" method where the feature space is (μ_{high}, $\mu_{\text{low}}/\mu_{\text{high}}$).

However, this two-component characterization is limited. Because of the spectral dependencies of the μ values, the ratio values depend not only on Z, but also on the spectrum. Specifically, DECT systems typically use X-ray tube sources that generate a wide spectrum of radiation. Lower-energy X-rays tend to be preferentially absorbed over higher-energy X-rays, which leads to spectral changes (beam-hardening) through the object. Along with scatter, this beam-hardening results in the common "cupping artifact" [4]. Beam-hardening compensation (BHC) [4] based on a reference material such as water may be applied, but the resulting attenuation coefficient value is then tuned to that reference material. No single BHC reference is universally applicable across a wide range of specimen ρ or Z values. Incorrect BHC is an important source of error in determining the absolute chemical makeup of materials.

B. Photoelectric-Compton Decomposition—(a_p, a_c)

Alvarez and Macovski [1] showed that dual-energy attenuation in the 30 to 200 keV energy range can be approximately decomposed into two components—photoelectric absorption and Compton scatter—that describe the energy-dependence of the X-ray attenuation coefficients as follows:

$$\mu(E) = (E^{-3})a_p + f_{KN}(E)a_c \tag{1}$$

where a_p and a_c are material-dependent photoelectric and Compton attenuation coefficients, E is the X-ray energy of interest in keV, and $f_{KN}(E)$ is the Klein-Nishina formula [25] for free-electron Compton scattering given as

$$f_{KN}(E) = \frac{1+\alpha}{\alpha^2}\left[\frac{2(1+\alpha)}{1+2\alpha} - \frac{1}{\alpha}\ln(1+2\alpha)\right] + \frac{1}{2\alpha}\ln(1+2\alpha) - \frac{1+3\alpha}{(1+2\alpha)^2} \tag{2}$$

where $\alpha = E/m_e$ and m_e is the rest mass of the electron (510.999 keV according to NIST). They showed that a_p and a_c could be approximated with two mono-energetic scans that could provide useful independent pieces of information.

C. Effective Atomic Number and μ_{high}—(μ_{high}, Z_{eff})

Ying, Naidu and Crawford (YNC) [2] further extended this technique to produce a measure of Z_{eff} from DECT, using the (μ_{high}, Z_{eff}) feature space to improve material characterization relative to at least three reference materials. YNC also proposed additional scatter, streak and spectral corrections for explosives detection in aviation security.

Z_{eff} is used in many DECT applications, and software exists to calculate it [26]. The commonly-used definition of Z_{eff} that stems from a 1937 paper [10] is

$$Z_{\text{eff}} = \sqrt[p]{\sum\nolimits_{i=1}^{N} r_i Z_i^p} \tag{3}$$

where N is the number of constituent elements in the material and, for each element i, Z_i is its atomic number and r_i is its "relative electron fraction" contribution. The relative electron fraction of a constituent element is defined as:

$$r_i = \frac{n_i Z_i}{\sum_{j=1}^{N} n_j Z_j}, \tag{4}$$

where n_i is the number of atoms having atomic number Z_i. The exponent p (originally set to 2.94, although other values have been used) should be optimized depending on the materials, spectral region and system specifics. For this paper, p is set to 3.80, per the sponsor's direction. As we will show, a fundamental problem with the Z_{eff} formulation is that (3) is not specifically tied to the absorption properties. Thus, optimizing its p value for one calibration set does not guarantee a match to other materials not in that set.

Manipulating the equations presented in [1], YNC calculates an approximate Z_{eff} image from photoelectric and high-energy attenuation images by the following equation:

$$\hat{Z}_{\text{eff}} = k\left(\frac{a_p}{\mu_{high}}\right)^{1/n} \tag{5}$$

where k and n are constant coefficients found by calibration against a set of reference materials with known Z_{eff} values. Then YNC uses a feature space of (μ_{high}, Z_{eff}) where, like the Ratio method, μ_{high} is used as a surrogate for the density of the material.

Z_{eff} is an improvement on the low/high-energy attenuation ratio, but it is still limited because of its ill-defined connection to a material's X-ray properties. Materials with identical Z_{eff} can often demonstrate different X-ray attenuation. This problem occurs regardless of the selected value of exponent p in (3), which cannot be chosen to fit all compounds and mixtures to their X-ray responses equally well. Also, this method does not overcome the same limitations found in the Ratio method of using μ_{high} as an approximation to density.

D. Electron Density and Effective Atomic Number—(ρ_e, Z_e)

A new feature space of ($\rho_{\mathbf{e}}$, $Z_{\mathbf{e}}$) can be derived where the two parameters reflect the X-ray transmission properties of materials in the energy and Z range of interest. By being directly associated with X-ray cross sections, this feature space is closer to actual material properties so that the results will be less dependent on system or spectrum.

1) $\rho_{\mathbf{e}}$ Definition and Estimation : X-ray absorption is directly proportional to a material's electron density, $\rho_{\mathbf{e}}$ [27]. In contrast, the material's *mass density*, ρ, does not directly govern how X-rays are attenuated, even though it is easily calculated from weight and volume measurements [28]. The electron density of a material, given as the number of electrons per unit

volume (electron-mole/cm^3 or moles-e$^-$/cm^3), can be derived from its mass density as follows:

$$\rho_e = \sum_{i=1}^{N} \frac{Z_i}{A_i} \rho \tag{6}$$

where A_i is the atomic mass and Z_i is the atomic number for element i as in (4). Because of its direct proportionality to the Compton component, which dominates X-ray attenuation at these energies, an estimate of ρ_e can be calculated as follows from [1]:

$$\hat{\rho}_e = K a_c, \tag{7}$$

where K is a constant coefficient that can be calibrated from the reference materials as is done for Z_{eff}.

2) Z_e Definition and Estimation : The Z_e effective atomic number model describes an arbitrary material by its total X-ray cross section, which is what affects the attenuation of impinging X-rays. Elemental cross section values have been measured and tabulated in [29]. From these values, we derive the total electronic cross section (the sum of photoelectric, incoherent and coherent) for pure elements up to $Z = 100$ and at photon energies from 10 keV to 500 keV. We denote $\sigma_e(Z, E)$ as the total electronic X-ray cross section (cm^2/electron-mole) of the element Z for X-ray energy E. Then the X-ray transmission value $T_Y(E)$ for a specified material Y, which could be a molecular compound or a mixture of compounds consisting of N elements, follows the Beer-Lambert law

$$T_Y(E) = \exp\left[-M_Y \sum\nolimits_{i=1}^{N} r_i \sigma_e(Z_i, E)\right] \tag{8}$$

where M_Y is the areal electron density of Y, and r_i and Z_i are the relative electron fraction and atomic number, respectively, for element i as in (4).

Then the Z_e of material Y can be defined as a fractional (non-integer) "atomic number" of an artificial element whose cross section and transmission would be optimally close to that of Y. Define the transmission for this artificial Z_e element in terms of a calculated cross section, $\sigma_{Ze}(E)$, and the areal electron density of the material Y, M_Y, as in (8):

$$T_{Ze}(E) = \exp\left[-M_Y \sigma_{Ze}(E)\right]. \tag{9}$$

where the simulated electronic cross section $\sigma_{Ze}(E)$ is based on two adjacent elements Z and $Z+1$ in the periodic table:

$$\sigma_{Ze}(E) = (1-\delta)\sigma_e(Z, E) + \delta\sigma_e(Z+1, E) \tag{10}$$

and δ is a fractional part of Z_e between 0 and 1 (e.g., if $Z_e = 8.3$, Z is 8 and δ is 0.3). A least-squares optimization of the X-ray transmission error compared to the tabulated values in [29] finds the best-fit Z_e value that minimizes the following equation over all E in the spectral range of interest:

$$Z_e = \arg\min_{Z_e} \left\{ \int \left[T_{Ze}(E) - T_Y(E)\right]^2 dE \right\}. \tag{11}$$

In this way, the artificial Z_e material will have X-ray attenuation properties that are optimally (in the least squares sense) close to a mixture of the pure elements that are nearest Z_e in the periodic table.

One caution in using Z_e or any other effective-Z estimate is that it becomes spectrally sensitive near material absorption edges. A material with a strong absorption edge in the energy range of interest is not accurately described by any type of effective-Z.

The estimation of Z_e from photoelectric and Compton attenuation images can be performed with the same calibration relative to reference materials as is done for Z_{eff} in (5), but instead using a_c in the denominator,

$$\hat{Z}_e = k' \left(\frac{a_p}{a_c}\right)^{1/n'} \tag{12}$$

where k' and n' are different constant coefficients than in (5) as they are calibrated against the known Z_e values (not Z_{eff}) of the reference materials. A Java application called ZeCalc [30] (available from LLNL under limited license by DHS) calculates optimal estimates of Z_e and ρ_e for a material of known chemical composition with known density and a specified energy range (10 to 500 keV). ZeCalc also displays the system spectral response compared to the Z_e transmission spectrum so that the user is made aware of possible spectral fit inaccuracies near absorption edges.

3) Differences between Z_e and Z_{eff} : Unlike Z_{eff} as defined in (3), which contains no cross section component, the Z_e model can be thought of as one whose radiographic response to narrow-beam polyenergetic X-rays is most similar to the material of interest. Two materials with identical Z_e will have closer X-ray cross sections than materials with identical Z_{eff}. Also, Z_e can be tailored to the spectrum of interest so it is well-suited to radiographic applications such as DECT where absolute material characterization accuracy is often needed.

To demonstrate these differences, values of Z_e (at 100 kV and 160 kV endpoint voltages) and Z_{eff} (using $p = 3.8$) for some common materials are listed in Table I. In this report, polyoxymethylene (POM) is an acetyl copolymer resin that is similar to the acetyl homopolymer known by the brand name Delrin by DuPont Co. Polytetrafluoroethylene (PTFE) is a synthetic fluoropolymer of tetrafluoroethylene that is identical in composition to Teflon by DuPont Co, and PVC is polyvinyl chloride. The last two materials in the table, lithium bromide (LiBr) and rubidium bromide (RbBr), provide a way to create aqueous alkali-halide solutions that have repeatable, known, adjustable, and precise (ρ_e, Z_e) values over a range of Z_e values.

For the lower effective-Z materials, the sets of Z_{eff} and Z_e values are very similar. However, for higher-Z materials (e.g., the last two rows in Table I) Z_{eff} diverges by over 10%. For example, the 19% RbBr solution demonstrates X-ray attenuation that is very close to pure calcium ($Z = 20$) as estimated by Z_e, and very different from titanium ($Z = 22$) as estimated by Z_{eff}. As pointed out in Section II-C, one could select a value for the exponent p in (3) that will improve the Z_{eff} numbers for a limited range of materials and energies. However, there is not one p value that will work for all cases.

III. SIRZ Method

A new method called System-Independent Rho-e/Z-e (ρ_e/Z_e) or SIRZ is a way to compute the (ρ_e, Z_e) features

TABLE I
CALCULATIONS OF Z_e AND Z_{eff} FOR SELECTED MATERIALS

Material[a]	Formula	ρ g/cm^3	ρ_e [b]	Z_e @ 100kV	Z_e @ 160kV	Z_{eff} p=3.8
Lexan	$C_{15}H_{16}O_2$	1.21	0.647	6.12	6.07	6.19
POM	$(CH_2O)_n$	1.42	0.754	7.01	6.97	7.07
Water	H_2O	1.00	0.554	7.44	7.39	7.54
PTFE	$(C_2F_4)_n$	2.20	1.056	8.43	8.43	8.50
Silica	SiO_2	2.65	1.323	11.64	11.62	11.85
PVC	$(C_2H_3Cl)_n$	1.35	0.691	14.07	14.06	14.44
12% LiBr	$LiBr/H_2O$	1.05	0.565	16.43	16.57	18.68
19% RbBr	$RbBr/H_2O$	1.17	0.623	19.95	20.08	22.18

[a] The percentage by weight of lithium bromide (LiBr) or rubidium bromide (RbBr) are in aqueous solutions (bottom two rows).

[b] The electron density ρ_e values are in units of moles-e$^-$/cm^3.

and is an extension of the method proposed by YNC [2]. SIRZ starts with the sinograms of low- and high-energy logarithmic projections, P_L and P_H respectively, produced by DECT scanners. These sinograms can be reconstructed by convolution-backprojection (CBP) or other CT algorithms into linear-attenuation-coefficient images used by the Ratio method (μ_{low} and μ_{high}) [31]. For SIRZ, the sinograms are decomposed into photoelectric and Compton parts using estimates of the system spectral response followed by conversion to the (ρ_e, Z_e) space.

A. Photoelectric-Compton Decomposition

The P_L and P_H sinograms are related to photoelectric and Compton contributions through (1) and by extension of the Beer-Lambert law to polychromatic sources

$$P_L = -\ln\left\{\int S_L(E)\exp\left[-\left(E^{-3}\right)A_p - f_{KN}(E)A_c\right]dE\right\} + \ln\int S_L(E)dE \quad (13)$$

$$P_H = -\ln\left\{\int S_H(E)\exp\left[-\left(E^{-3}\right)A_p - f_{KN}(E)A_c\right]dE\right\} + \ln\int S_H(E)dE \quad (14)$$

where A_p and A_c are line-integral sinograms of photoelectric and Compton radiographic attenuation coefficients, respectively, and S_L and S_H are the low- and high-energy X-ray system spectral responses (source and detector) as a function of energy (in keV) described in the next section.

To solve for A_p and A_c, we use a constrained minimization method that employs modeled system spectral responses in (13) and (14). Each A_p and A_c projection value is computed using a two-dimensional Newton-Raphson technique with non-negativity constraints on the solution. If a low- or high-energy projection value is less than or equal to zero, suggesting the absence of an attenuating region, the resulting photoelectric and Compton projection values are set to zero. When optimization yields a negative photoelectric or Compton projection value, which describes a non-physical outcome, a Newton-Gauss optimization is performed under the added constraint that either A_p or A_c is equal to zero, which guarantees the complementary value to be positive. The resulting pair that minimizes the mean squared error between back-computed projection values and observed projection values is preserved.

The resulting A_p and A_c sinograms are reconstructed into photoelectric (a_p) and Compton (a_c) attenuation-coefficient images, again using CBP or equivalent.

B. System Spectral Response Estimation

The SIRZ algorithm relies on knowledge of the "system spectral responses," $S_L(E)$ of (13) and $S_H(E)$ of (14), which are defined as the product of the X-ray source spectrum and the detector spectral response for low- and high-energy spectra, respectively. In the experiments below, models of the system spectral responses are calculated for each energy-spectrum pair employed by each of the two DECT scanners. Since each scanner has similar yet different X-ray source, filtration and detector hardware, each system spectral response model is also unique.

Detector spectral response models are estimated by building detailed MCNP6 [32] models of the detectors using full electron-photon transport to simulate energy deposition in the detector. The two DECT scanners employed in the experiments below utilize flat-panel array detectors from two different vendors, but the modeling process is done the same way. Using vendor-supplied specifications, the models include all detector materials and thicknesses that the X-rays pass through. The energy deposition in the scintillator for all relevant photon energies is computed for incident photon pencil-beams of a selected energy. MCNP6 calculations are then performed over forty energy bands to provide coverage of the spectral range. This same method would also apply to other detector types and configurations such as linear detector arrays.

The X-ray source spectral models used to describe the two scanner systems in our experiments were based on different semi-empirical models even though the physical X-ray tube sources are the same type (Yxlon 450 kV D09 tube-head with tungsten target, 11-degree takeoff angle, 0.4-mm spot size, and 5.0-mm beryllium window). The systems are abbreviated as "HE" (for one housed at a High-Explosives Application Facility) and as "TB" for testbed because it is reconfigurable (located in a different building). For HE, we used a model by Finkelshtein and Pavlova [33] whereas for TB we used a model by Poludniowski and Evans [34]. Both models are adequate and comparable in accuracy to MCNP6 models while being simpler and faster to implement. The models assume tungsten-anode sources with beryllium windows and with adjustable endpoint voltages, X-ray filtration materials and thicknesses. Each modeled spectrum is optimized by making small adjustments in the modeled source filtration such that the transmission for the overall system spectral response, including the detector, matches the experimentally-measured transmissions for the specimens as a group.

C. Conversion to (ρ_e, Z_e) with Reference Materials

The final steps of SIRZ involve computing quantitative estimates of ρ_e and Z_e from the decomposed a_p and a_c values using (7) and (12) respectively. To compute the constant coefficients k', n' and K, calibration is done on a per-scan basis with a set of four reference materials that have known ρ_e and Z_e values and are scanned with the same spectral pairings as the specimens. Newton-Gauss optimization is used to estimate these coefficients in the minimum-mean-squared-error sense. [Note that for YNC, we use this same method to calculate k and n coefficients in (5) for calibrating the Z_{eff} estimation. In this way, the same data can be processed by both SIRZ and YNC for comparison purposes.]

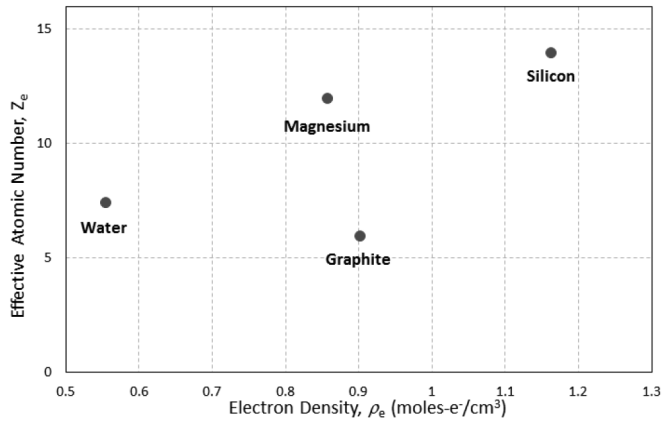

Fig. 1. The four reference materials used in the experimental studies were selected to cover a prescribed range of the (ρ_e, Z_e) feature space.

TABLE II
REFERENCE MATERIALS SCANNED IN THE DECT EXPERIMENTS

Reference Material	Chemical Makeup	Bulk Density, ρ (g/ cm^3)	Electron Density, ρ_e (moles-e$^-$/cm^3)	Effective Atomic Number[a], Z_e
Graphite	C	1.80 ± 0.01	0.901 ± 0.003	6.00 ± 0.01
Water[b]	H_2O	1.00 ± 0.01	0.554 ± 0.002	7.43 ± 0.01
Magnesium	Mg	1.74 ± 0.02	0.857 ± 0.003	12.00 ± 0.01
Silicon	Si	2.33 ± 0.02	1.162 ± 0.003	14.00 ± 0.01

[a] Z_e values were supplied by ZeCalc [30] using a 160 keV endpoint spectrum and a nominal areal density of $2.5\ \mathrm{g/cm^2}$.

[b] De-ionized reagent-grade water (from Fisher Scientific, Cat # 23-751-610) is contained in a polyethylene bottle.

The reference materials were chosen to span the (ρ_e, Z_e) feature space of interest to security, medical and NDC applications. They were high-purity (typically $> 99.99\%$ of a single element or of well-known elemental and molecular composition) such that actual ρ_e and Z_e values can be reliably calculated using ZeCalc [30]. Table II lists the reference materials and their chemical and physical properties. The ρ_e values were from 0.56 to 1.16 moles-e$^-$/cm^3, and the Z_e values were from 6 to 14. Like the specimens in our experiments, they were independently certified with purity and trace element analyses. The four reference materials are plotted in (ρ_e, Z_e) feature space in Fig. 1.

Full image estimates of ρ_e and Z_e can be calculated with SIRZ for heterogeneous specimens. However, for homogeneous materials (like the reference materials and some specimens in the experiments below) the calculation need only be performed on scalar mean values for a_p and a_c in the object region. That way, the coefficient estimation above is done once per scan on the mean values inside each material region rather than calculating different estimates for each voxel.

IV. EXPERIMENTS TO TEST SYSTEM INDEPENDENCE

This section describes a series of experiments designed to test the system independence of results from Ratio, YNC and SIRZ methods of DECT processing. Using the HE and TB scanners and five pairs of spectral ranges with endpoint energies from 80 to 200 keV, we scanned several well-characterized specimens so our study could focus on the extent of sensitivity to the spectral differences by comparing to ground truth.

TABLE III
HOMOGENEOUS SPECIMENS USED IN THE DECT EXPERIMENTS

Specimen	Diam. (mm)	Bulk Density, ρ (g/ cm^3)	Electron Density, ρ_e (moles-e$^-$/cm^3)	Effective Atomic Number[b], Z_e
Graphite	50.9	1.68 ± 0.01	0.840 ± 0.003	6.00 ± 0.01
Water[a]	36.9 id 38.9 od	1.00 ± 0.01	0.554 ± 0.002	7.43 ± 0.01
PTFE	55.3	2.17 ± 0.02	1.042 ± 0.003	8.44 ± 0.01
Magnesium	25.3	1.74 ± 0.02	0.858 ± 0.003	12.00 ± 0.01
Silicon	25.3	2.33 ± 0.02	1.161 ± 0.003	14.00 ± 0.01

[a] The water was contained in a high-density polyethylene bottle with inner and outer diameters listed; density and Z_e numbers are for water alone.

[b] Z_e values were supplied by ZeCalc [30] using a 160 keV endpoint spectrum and a nominal areal density of $2.5\ \mathrm{g/cm^2}$.

A. Specimens

The specimens were chosen such that they (1) had known ρ_e, and Z_e so we could test the extent of system independence of the DECT results and (2) were of suitable size and composition to be imaged (transmitted) by all the test spectra and scanners without being dominated by noise, scatter and other CT issues. This second restriction means that we attempted to keep the maximum X-ray transmission values ($\ln(\mu L)$) near 2 as suggested by [35], where L is the thickness of the specimen. Our preferred transmission range is 1 to 2, and artifacts and poor statistics make analysis difficult beyond 4. In the end, the specimens fell into three different classes—homogeneous, heterogeneous and high-Z—and of them all, only the 80-keV-endpoint scan of the high-Z specimen (defined in IV-A3 below) exceeds 3 at 3.58. Still, beam hardening artifacts were observed in the high-Z specimen even in the highest-keV scan suggesting that any DECT processing would be challenged by this specimen (as intended).

1) Homogeneous Specimens: A set of homogeneous specimens were fabricated as listed in Table III. Notice that the graphite specimen density is about 7% less than that of the graphite reference material in Table II, which will be important in the Results section. The 1.27-cm homogeneous regions in the heterogeneous specimen (shown next) are also considered homogeneous specimens in order to have more samples for analysis.

2) Heterogeneous Specimens: A more difficult challenge is to measure the (ρ_e, Z_e) values of multiple materials in heterogeneous specimens. In this case, the two heterogeneous specimens are 5-cm (outer diameter) cylinders of PTFE and POM that have four machined half-inch holes (1.27-cm diameter) filled with other inserted materials or air (empty). The PTFE-based heterogeneous specimen is schematically shown in Fig. 2 along with its CT reconstruction. The POM-based heterogeneous specimen (not shown) has the same inserts as Fig. 2 except that PTFE replaces the POM insert. All materials are well-characterized and have similar values to corresponding reference materials and homogeneous specimens.

3) High-Z Specimen: To test the extrapolation limits of the SIRZ algorithm, a high-Z specimen was designed to fall outside the (ρ_e, Z_e) calibration range of the reference materials. This high-Z specimen is a 19% (by weight) rubidium bromide (RbBr) aqueous solution (prepared in a specimen

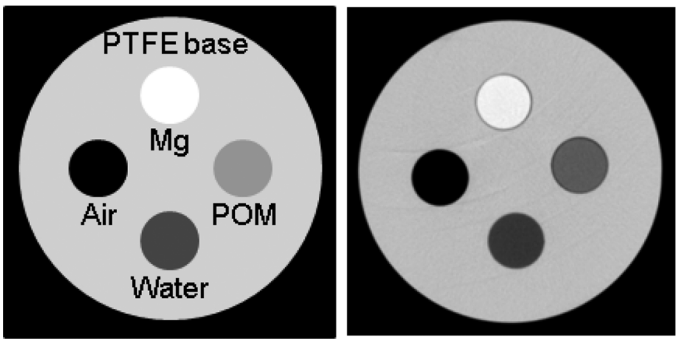

Fig. 2. Design (left) and CT reconstruction (right) at 100 keV (endpoint; 1.96-mm Al filter) of the PTFE-based heterogeneous specimen with 5-cm outer diameter. The PTFE base has four 1.27-cm diameter holes filled with inserts of magnesium, POM, water and air (empty). All holes have floors to contain the insert or liquid, so no separate container was used for the water "insert".

bottle) that exhibits a composite Z_e of 20.05 ± 0.05 and ρ_e of 0.623 ± 0.003 moles-e^-/cm^3 as calculated by ZeCalc [30]. Compared to the reference materials depicted in Table II and Fig. 1, this specimen lies much higher in Z_e (off the chart) and it has a ρ_e between water and POM.

B. DECT Systems Used

We used two similar industrial CT systems [36]–[38] designed to characterize small (up to 30-cm outer diameter) material specimens. The HE and TB systems (defined in Section III-B) had similar fixed geometries, identical rotating specimen holders or "carousels," and the same type of X-ray tube source. The main difference between the two CT systems was the different flat-panel amorphous-silicon detectors used; the HE system had a Thales Flashscan 33 detector, and the TB system had a PerkinElmer XRD 1620 detector. The Thales detector contained 3200×2240 detector elements of size 0.127 mm $\times$ 0.127 mm. Detector elements were binned for the data acquisition to 2133×1493 at 0.1905 mm $\times$ 0.1905 mm. The scintillator to convert the X-rays to visible light was a Lanex Fine $Gd_2O_2S:Tb$. The PerkinElmer panel contained 2048×2048 detector elements of size 0.200 mm $\times$ 0.200 mm, so no pixel-binning was applied. The scintillator was a DRZ Plus $Gd_2O_2S:Tb$.

The CT geometry of both systems is shown schematically from the side in Fig. 3. For each stepped angle of the carousel, a 2D projection image on the detector is processed down to two linear (1D) slit projections of X-ray transmission—one for the specimen (upper level) and another for the half-inch-diameter (1.27 cm) reference materials (lower level). The two narrow slits in the second collimator define these two projection regions and serve to reduce out-of-plane scatter and detector blur. A complete 360-degree carousel rotation of stepped projections with one energy spectrum produces upper and lower sinograms that are reconstructed into the two cross-sectional (μ) images as shown in Fig. 4. This process is repeated for each source spectrum to be acquired. An identical set of carousel, specimens and reference materials was used on both HE and TB systems.

C. Scans Performed

Experiments involved scanning all of the three types of specimens of different sizes on the two CT systems (HE and TB) using multiple pairs of energy spectra [39]. The endpoint voltages and X-ray source filters employed are shown in Table IV. On the TB scanner, all of the specimens were scanned and CT data were acquired using all five spectra. Due to scanner availability, the specimens were scanned with only two spectra (100 keV and 160 keV) on the HE scanner. These two spectral ranges are most commonly used in medical and security DECT. Due to the spectral response differences of the two detectors involved, the source filters also differed in order to optimize the total spectral responses of each scanner.

The same data acquisition procedures were performed for each spectrum on each scanner and with the same starting rotation angle to ensure image registration. The steps included system alignment, source quality checks, detector calibration, background and dark-current measurement, and acquisition of specimen and reference-material sinograms. In each case, 720

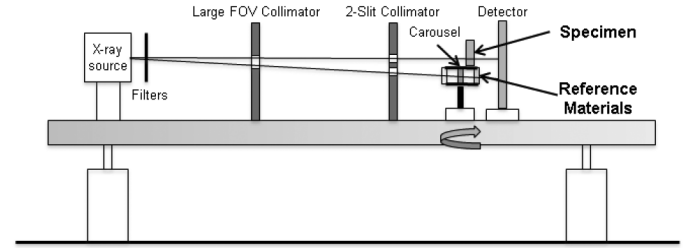

Fig. 3. HE and TB CT system schematic viewed from the side. The carousel rotates about the vertical axis to expose the specimen and reference materials (in two different slits) from all angles. The detector is a flat-panel array, which is only illuminated by the slits in two horizontal rows (into the page).

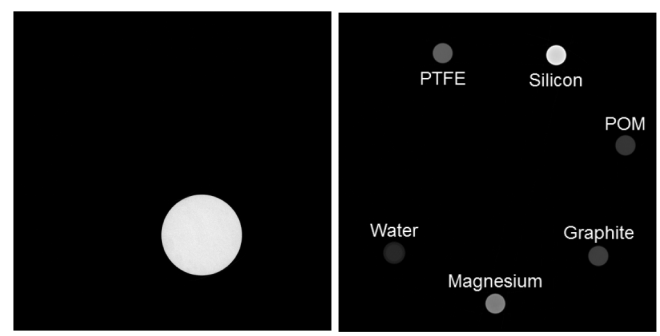

Fig. 4. Example CT reconstructions of a 5.09-cm diameter graphite specimen (left) and the 1.27-cm diameter reference materials (right). The X-ray source had 100-keV-endpoint energy and a 1.96-mm-thick aluminum filter. Cupping artifacts are visible in the magnesium and silicon references. Note that data from POM and PTFE reference materials were not used in calibration.

TABLE IV
CT SCANNERS, SPECTRA AND FILTERS USED IN EXPERIMENTS

		Endpoint Energy (keV)[a] Filter Thickness (mm)				
CT Scanner	**Filter**	**80**	**100**	**125**	**160**	**200**
HE	Aluminum		1.94		1.94	
	Copper		0		1.91	
TB	Aluminum	0.41	1.96	0	1.96	0
	Copper	0	0	0.92	1.85	2.87
	Steel	0.13	0	0	0	0

[a] The shaded boxes indicate the scans that were not acquired.

equi-angular 1D projections were acquired over 360 degrees of rotation. The specimens are in keyed holders that keep registration error below one-quarter of a voxel ($\sim 50\ \mu$m).

The CT preprocessing algorithms performed after acquisition were consistent for all experiments [38]. To compare with commonly-used methods, the data were reconstructed into low- and high-energy μ-images such as the 100-keV μ-images in Fig. 4 using a convolution backprojection algorithm. For the Ratio method only, the 100-keV projections that were reconstructed into 100-keV μ-images were processed for beam-hardening compensation using water-referenced BHC coefficients. For YNC and SIRZ methods, no BHC steps were performed.

All μ values reported in this paper are given in "Modified Hounsfield Units" commonly used in security CT, where air is set to a value of zero and water is set to 1000.

D. DECT Processing Methods

Because many spectral data sets were acquired on TB of the same specimens, several dual-energy pairings could be defined and processed as different DECT scans. For ease of notation, we denote each pairing by the two-letter scanner name followed by the low and high endpoint voltages used. Five particular pairings were compared against one another: HE100/160, TB100/160, TB80/125, TB125/200, and TB80/200. These five pairings can each be considered as a different dual-energy scanner with widely-varying spectral ranges (except for the first two, which are different physical scanners) so that we can test for system and spectral independence of the results.

The three different DECT processing methods we have discussed were performed and compared:

- Ratio – feature space is ($\mu_{\rm high}$, $\mu_{\rm low}/\mu_{\rm high}$);
- YNC – feature space is ($\mu_{\rm high}$, $Z_{\rm eff}$) as in [2];
- SIRZ – feature space is ($\rho_{\rm e}$, $Z_{\rm e}$).

The YNC method we implemented is our best understanding of the published method with one difference; we used all four reference materials for calibration, whereas YNC used three different reference materials. The coefficients in (5), (7) and (12) were recalculated for each spectral pairing using the same four reference materials.

The feature values were calculated from the means and standard deviations of the hundreds of voxels representing the specimen or reference materials by the following method. Starting with the Compton images, which had the lowest noise and were co-registered with the others, a threshold was selected to establish binary segmentation masks for each image region. The binary segmentation masks were then sent to an active-contour segmentation algorithm to generate a secondary binary mask [40], [41]. In order to remove partial-volume and container voxels at the edges, multiple iterations of a 3×3-square morphological erosion function were applied to the secondary binary mask. Specimens were subjected to 15 iterations, whereas the solid and liquid reference materials were subjected to four and 13 iterations, respectively. The resulting segmented and eroded Compton binary masks were used to extract the material voxels from both photoelectric and Compton images. The mean and standard deviation values of the extracted (masked) voxels for each material were tabulated and analyzed in this study. The numbers of DECT extracted regions analyzed varied by specimen from five (for graphite, silicon and RbBr) to ten (for POM) to fifteen (for water, PTFE, and magnesium). All sample uncertainties are reported as one standard deviation root-mean-square (RMS).

For the heterogeneous specimens, the three non-air regions were segmented and processed individually; those results were included with the others of like homogeneous materials. We also defined a fourth circular region in the centers of the heterogeneous specimens and of the same size as the inserts (1.27-cm), which were included with the others of like homogeneous materials—i.e., PTFE for the PTFE-based specimen and POM for the POM-based specimen. By including these regions with the homogeneous specimens, we can investigate how the presence of diverse materials in the X-ray plane affects robustness to heterogeneity in specimens.

V. Results

In this section, we display the feature-space plots for Ratio, YNC, and SIRZ. Then we explore the precision and accuracy of each method, and the spectral stability of SIRZ.

A. Feature-space Plots for All Specimens

The feature-space plots for Ratio, YNC, and SIRZ are shown in Figs. 5–7. The error bars are one standard deviation, or one-sigma (RMS variation), about the calculated mean values of all measurements for each material.

Since ground-truth $\rho_{\rm e}$ and $Z_{\rm e}$ values are known for all the specimens, the SIRZ plot in Fig. 7 displays the "Actual" values (as open diamonds). Note that the graphite *specimen* in Fig. 7 is shifted left from the graphite *reference material* in Fig. 1 because the two physical objects have slightly different bulk densities as noted before. The other two plots do not display "Actual" values because the $\mu_{\rm high}$ and Ratio quantities differ between spectra and scanners so the ground truth is unknown.

B. Precision Results

The Ratio method results in Fig. 5 demonstrate that the $\mu_{\rm low}$ and $\mu_{\rm high}$ features have broad error bars that are even larger at higher densities and Z (e.g., for silicon and RbBr). The YNC method in Fig. 6 shows improvement for the lower Z materials (below magnesium), but it suffers from the same wide range in $\mu_{\rm high}$ as does Ratio, which limits the system-independence of the YNC results. SIRZ results demonstrate tight clusters around each specimen material with the exception of RbBr. The standard deviations in percent for each of the relevant features and each specimen material are shown in Table V.

This table shows numerically what can be seen visually in the three prior figures. The large errors for the Ratio method (8.9% for graphite to 24.5% for RbBR) are expected given the widely-varying spectra we used, which exaggerate the system differences and show that the Ratio features are problematic for dissimilar or changing DECT systems. Yet the Ratio method is still commonly in use. The standard deviations of $\rho_{\rm e}$, $Z_{\rm e}$, and $Z_{\rm eff}$ estimates are much lower than the μ-based features—they are all $< 2\%$ and consistent across specimens (with the exception of RbBr). That is, the YNC clusters in Fig. 6 are compact in the $Z_{\rm eff}$ direction but not in $\mu_{\rm high}$, and the SIRZ clusters in Fig. 7 are compact in both $\rho_{\rm e}$ and $Z_{\rm e}$.

The RbBr specimen has an uncertainty spread that is visibly larger than the others within each method's feature space for two

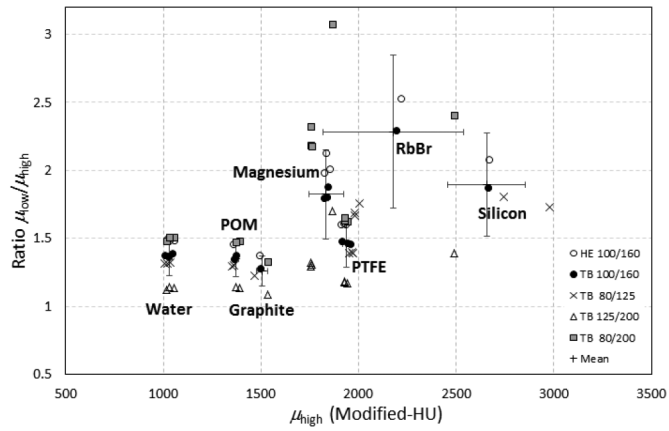

Fig. 5. Ratio feature space for all materials using the five spectral pairs.

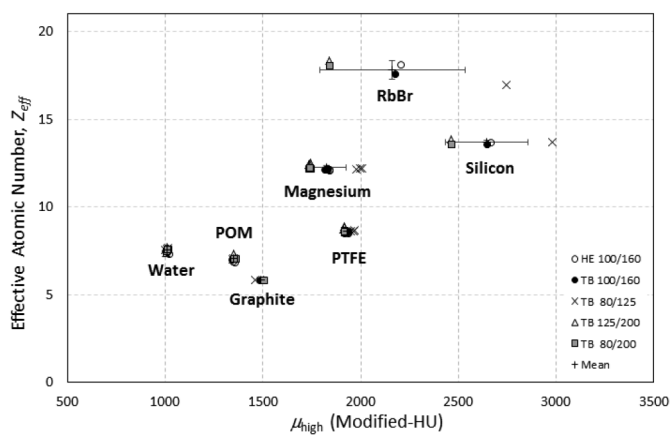

Fig. 6. YNC feature space for all materials using the five spectral pairs.

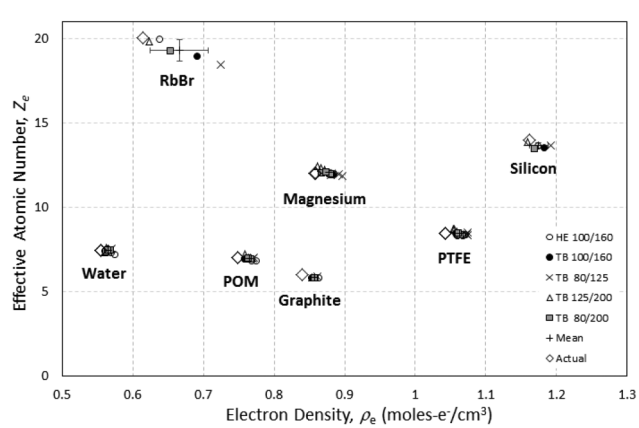

Fig. 7. SIRZ feature space for all materials using the five spectral pairs.

possible reasons: (1) it is out of the (ρ_e, Z_e) range of the reference materials so the estimates are extrapolated and (2) it is higher attenuating, so there is lower X-ray transmission leading to higher noise. Still, SIRZ generates precision numbers of 6.2% and 3.3% in estimated ρ_e and Z_e, respectively, compared to greater than 17% for μ_{high} used in Ratio and YNC.

C. Accuracy Results

The difference between a feature estimate and its ground-truth or "actual" value is a measure of accuracy. Since the attenuation coefficients change with scanner and spectrum, only the estimates of ρ_e, Z_e (from SIRZ) and Z_{eff} (from YNC) have baseline actual values for accuracy comparisons across spectra and materials. The maximum and mean values of absolute errors (in percent) for these features are listed in Table VI for each of the specimen materials. The Z_e accuracy errors are below 3% except for the RbBr outlier. The Z_{eff} accuracy errors are often larger but comparable to those of Z_e while the RbBr outlier is much larger (over 20%) because, as we saw in Table I, Z_{eff} is ill-defined in that region. Note that we used $p = 3.80$ in (3) for ground-truth values of Z_{eff}. Accuracy errors for ρ_e are larger in general, but the means are still below 3% for all but RbBr. These errors in ρ_e are from a consistent bias visible in Fig. 7 (the actual values lie to the left of each cluster). This bias may be due to several factors including differences in the upper (specimen) and lower (reference) slit measurements or to approximations inherent in the basis functions of (1) used to represent the total cross section.

In actuality, the two CT systems we used are very stable and similar in measuring μ_{high} despite their different detectors. (The μ_{low} values are more different depending on the spectrum.) The RMS variation in μ_{high} and ratio for the common 100/160 keV scans alone were less than 0.6% between HE and TB. We attribute this observation to the comparable spectral designs of the two systems even if the detectors differ. Some of the other spec-

TABLE V
STANDARD DEVIATION (IN %) FOR THE SPECIMENS

Precision (%) for Specimen[a]	Ratio	YNC		SIRZ	
	μ_{low}/μ_{high}	μ_{high}	Z_{eff}	ρ_e	Z_e
Graphite	8.9	1.1	0.3	0.5	0.3
POM	9.7	0.4	1.8	0.7	1.6
Water	10.1	0.5	1.4	0.7	1.3
PTFE	11.9	0.9	1.3	0.7	1.4
Magnesium	18.0	5.3	1.0	1.0	1.4
Silicon	20.0	8.0	0.9	1.1	1.1
19% RbBr	24.5	17.1	3.1	6.2	3.3

[a] The water, magnesium, POM and PTFE estimates include results of the relevant homogeneous regions from the heterogeneous specimens.

TABLE VI
ACCURACY (RMS ERROR IN %) FOR THE SPECIMENS

Accuracy (%) for Specimen[a]	ρ_e error[b]		Z_e error[b]		Z_{eff} error[c]	
	Mean	Max	Mean	Max	Mean	Max
Graphite	2.1	2.7	2.5	2.6	2.9	3.1
POM	2.3	3.4	0.3	3.5	1.8	3.8
Water	2.0	3.6	0.3	2.5	0.2	3.0
PTFE	2.0	3.1	0.3	3.6	1.7	4.6
Magnesium	2.3	4.4	0.5	3.7	2.0	4.4
Silicon	1.2	2.7	2.5	3.7	2.3	3.0
19% RbBr	8.4	18.0	3.8	8.1	20.0	23.5

[a] The water, magnesium, POM and PTFE estimates include results from the relevant homogeneous regions in the heterogeneous specimens.
[b] The ρ_e, and Z_e errors are from SIRZ estimates compared to ZeCalc.
[c] The Z_{eff} errors are from YNC estimates compared to (3) with $p = 3.80$.

TABLE VII
ERRORS CAUSED BY INACCURATE SYSTEM SPECTRAL RESPONSE MODELS

Max % absolute error given a →		5% Filter thickness change on		5 kV endpoint voltage change on	
		100kV	160kV	100kV	160kV
Without RbBr	Z_e	0.2	0.4	1.3	0.8
	ρ_e	0.4	1.0	2.7	1.6
With RbBr	Z_e	0.3	1.2	2.4	3.4
	ρ_e	0.5	4.2	11.0	9.4

tral pairings (such as TB80/125, TB125/200 and TB80/200) are far from optimal, yet SIRZ still performed well.

D. Sensitivity to the System Spectral Response Models

Given the spectral uncertainty for X-ray tube sources and detectors, we were interested to determine what happens to SIRZ if the system spectral response model is incorrect. Would the SIRZ performance be unstable or degrade with an inaccurate system spectral response model?

In order to answer this question, we used the above set of controlled measurements to test the sensitivity of SIRZ (not Ratio or YNC) to inaccuracies in system spectral response models. We performed two types of model perturbations when processing the 100-kV and 160-kV endpoint data—either the modeled endpoint voltage was changed by ± 5 kV or the filter thickness of one of the spectral models was varied by up to $\pm 5\%$. We varied only one of the spectral response models (either the 100-kV or the 160-kV spectrum) individually, while the other was kept at the nominal spectrum and processed normally through SIRZ. Note that these perturbations are large compared to most manufacturers' specifications (which are in the $\pm 1\%$ range), so our sensitivity tests are conservative measurements. The maximum absolute error results (in percent of actual) are shown in Table VII (for SIRZ only).

For each perturbation, the SIRZ calculations were carried out to produce the (ρ_e, Z_e) feature space and uncertainties were measured in the same way as before, and then aggregated over all specimens. We computed the absolute difference between the perturbed and unperturbed results, and then calculated the maximum percent difference.

Table VII shows that a 5% filter thickness change on the 100-kV spectrum causes little effect ($< 0.6\%$) even for RbBr. However, for the 160-kV spectrum, the effect is larger, up to 4.2% for RbBr. For the ± 5 kV endpoint voltage change without RbBr (top two rows), the errors are larger (up to 2.7%), and they are worse for ρ_e than Z_e. When the high-Z specimen (RbBr) is included (bottom two rows), the errors grow significantly (up to 11%) as was seen on the baseline SIRZ results. From these results, it appears that the system spectral response model needs to be known to roughly the same percentage error as the measurements themselves. Tuning the response to the known reference materials, as is done with SIRZ, can provide that kind of accuracy.

VI. DISCUSSION

The above results demonstrate how, using five different DECT data pairings from two different scanners, SIRZ shows precision errors of $< 2\%$ and accuracy errors of $< 3\%$ for test specimens whose Z is < 15. By contrast, the Ratio and YNC methods on the same data show precision numbers of up to 20% and 8% respectively.

For objects whose X-ray properties lie outside the span of the reference materials in the feature space (as with the RbBr solution that has effective Z of around 20) there is some loss in SIRZ performance as seen in Fig. 7 where accuracy and precision jump to 8.4% and 6.2%, respectively, which is still tighter than Ratio or YNC.

The DECT systems we used are able to scan the specimen and the reference materials simultaneously, but that is not a requirement. The reference material scans could be part of a periodic calibration procedure much like what is currently done in NDC, hospitals and airports. During the roughly nine weeks of intermittent scanning, in fact, we found that the standard deviation of the reference-material mean μ values averaged $< 0.5\%$ for all scans, except for the higher-Z references of magnesium and silicon that edged closer to 0.8 and 0.9%, respectively. A single set of reference values from one calibration procedure could have been used in our experiments and produced similar SIRZ accuracy and precision numbers.

We expect that the SIRZ technique can be extended and improved to a broader DECT domain. To validate such extensions, more thorough testing in (ρ_e, Z_e) feature space would be required. The choices of reference materials can be modified to extend SIRZ to, say, higher-energy regimes or higher-Z materials. These cases may require extension of the Z_e definition to account for absorption edges and pair production. Algorithm speed and the effects of image artifacts and scatter also need to be studied. Further tests using other types of DECT scanners (including commercial industrial, NDC, security and medical DECT scanners) with varied different materials are necessary to demonstrate that SIRZ and the (ρ_e, Z_e) feature space should be more broadly considered for DECT applications.

VII. CONCLUSION

Accurate and precise X-ray characterization of objects has been an important goal for NDC, security and medical applications. For X-ray characterization to be truly independent of the DECT scanning device, a technique and a feature space are required that encompass the physics of the measurement. We have introduced the SIRZ technique that can produce X-ray-relevant (ρ_e, Z_e) features that are accurate to $< 3\%$ and precise to $< 2\%$ when measured with different systems and spectra (at energies from 80 to 200 keV). To achieve these results, the SIRZ method relies on known reference materials that span the (ρ_e, Z_e) space and on accurate models of the source X-ray spectra and detector responses (that are calibrated to the known reference materials). Because the system spectral response is included, the X-ray beam-hardening is also inherently modeled in the process, so the standard correction methods are not needed. We also show that SIRZ is insensitive to imperfect estimates of the source spectrum and detector response.

ACKNOWLEDGMENT

The authors would like to acknowledge the efforts of S. DePiero, D. Grimsley, K. Morales, J. Montgomery, W. T. White, and A. Williams in preparing the specimens, acquiring X-ray data and carefully archiving the results to

be analyzed and described in this paper. They would like to thank the Thales Group and PerkinElmer, Inc., for providing details about their respective detector array panels. They would also like to thank J. Candy, C. Crawford, C. Divin, S. Glenn, R. Panas, W. T. White, G. Zarur, and C. Logan for their help in editing the manuscript.

REFERENCES

[1] R. E. Alvarez and A. Macovski, "Energy selective reconstructions in x-ray computerized tomography," *Phys. Med. Biol.*, vol. 21, no. 5, pp. 733–744, 1976.

[2] Z. Ying, R. Naidu, and C. R. Crawford, "Dual energy computed tomography for explosive detection," *J. X-ray Sci. and Tech.*, vol. 14, pp. 235–256, 2006.

[3] H. E. Martz, Jr., S. G. Azevedo, J. M. Brase, K. E. Waltjen, and D. J. Schneberk, "Computed tomography systems and their industrial applications," *Appl. Radiat. Isot.*, vol. 41, p. 943, 1990.

[4] H. H. Barrett and W. Swindell, *Radiological Imaging; The theory of image formation, detection, and processing*. New York, NY, USA: Academic, 1981.

[5] L. A. Lehmann, R. E. Alvarez, A. Macovski, W. R. Brody, N. J. Pelc, S. J. Riederer, and A. L. Hall, "Generalized image combinations in dual KVP digital radiography," *Med. Phys.*, vol. 8, no. 5, pp. 659–667, 1981.

[6] H. E. Martz, Jr., G. P. Roberson, D. J. Schneberk, and S. G. Azevedo, "Nuclear-spectroscopy-based, first-generation, computerized tomography scanners," *IEEE Trans. Nucl. Sci.*, vol. 38, no. 2, p. 623, Apr. 1991.

[7] Z. Qi, J. Zambelli, N. Bevins, and G. H. Chen, "Quantitative imaging of electron density and effective atomic number using phase contrast CT," *Phys. Med. Biol.*, vol. 55, pp. 6669–6677, 2010.

[8] H. E. Martz, Jr., G. P. Roberson, M. F. Skeate, D. J. Schneberk, and S. G. Azevedo, "Computed tomography studies of concrete samples," *Nucl. Inst. Meth.*, vol. B58, p. 216, 1991.

[9] L. Martin, W. C. Karl, and P. Ishwar, "Artifact reduction in dual-energy CT reconstruction for security applications," in *Proc. Third Int. Conf. Image Formation in X-ray Computed Tomography*, Jun. 2014, pp. 133–136.

[10] M. V. Mayneord, "The significance of the roentgen," *Acta of the International Union Against Cancer*, vol. ii, p. 271, 1937.

[11] W. A. Kalender, W. H. Perman, J. R. Vetter, and E. Klotz, "Evaluation of a prototype dual-energy computed tomographic apparatus. I. phantom studies," *Med. Phys.*, vol. 13, no. 3, pp. 334–339, May/Jun. 1986.

[12] P. Engler, W. D. Friedman, and E. E. Armstrong, "Determination of material composition using dual energy computed tomography on a medical scanner," in *Proc. ASNT Topical Conf. Industrial Computerized Tomography*, Jul. 1989, p. 142.

[13] H. E. Martz, Jr., D. J. Schneberk, S. G. Azevedo, and S. K. Lynch, "Computerized tomography of high explosives," in *Nondestructive Characterization of Materials, IV*, C. O. Ruud, Ed. *et al.* New York, NY, USA: Plenum, 1991.

[14] M. Iovea, M. Neagu, O. G. Duliu, and G. Mateiasi, "High accuracy x-ray dual-energy experiments and non-rotational tomography algorithm for explosives detection technique in luggage control," presented at the Int. Symp. Digital Industrial Radiology and Computed Tomography, Lyon, France, 2007.

[15] O. Semerci and E. L. Miller, "A parametric level-set approach to simultaneous object identification and background reconstruction for dual-energy computed tomography," *IEEE Trans. Image Process.*, vol. 21, no. 5, pp. 2719–2734, May 2012.

[16] T. P. Szczykutowicz, Z. Qi, and G. H. Chen, "A simple image based method for obtaining electron density and atomic number in dual energy CT," *Proc. SPIE Medical Imaging 2011: Physics of Medical Imaging*, vol. 1967, p. 79613A, Mar. 2011.

[17] J. S. Park and J. S. Kin, "Calculation of effective atomic number and normal density using a source weighting method in a dual energy x-ray inspection system," *J. Korean Phys. Soc.*, vol. 59, no. 4, pp. 2709–2713, Oct. 2011.

[18] G. Landry, J. Seco, M. Gaudreault, and F. Verhaegen, "Deriving effective atomic numbers from DECT based on a parameterization of the ratio of high and low linear attenuation coefficients," *Phys. Med. Biol.*, vol. 58, pp. 6851–6866, 2013.

[19] A. J. Gilbert, B. S. McDonald, R. M. Robinson, K. D. Jarman, T. A. White, and M. R. Deinert, "Non-invasive material discrimination using spectral x-ray radiography," *J. Appl. Phys.*, vol. 115, pp. 154301–1, 2014.

[20] R. R. Haghighi, S. Chatterjee, A. Vyas, P. Kumar, and S. Thulkar, "X-ray attenuation coefficient of mixtures: Inputs for dual energy CT," *Med. Phys.*, vol. 38, no. 10, pp. 5270–5279, 2011.

[21] B. J. Heismann, J. Leppert, and K. Stierstorfer, "Density and atomic number measurements with spectral x-ray attenuation method," *J. Appl. Phy.*, vol. 94, no. 3, pp. 2073–2079, 2003.

[22] P. M. Shikhaliev, "Energy-resolved computed tomography: First experimental results," *Phys. Med. Biol.*, vol. 53, pp. 5595–5613, 2008.

[23] C. Robert-Coutant, V. Moulin, R. Sauze, P. Rizo, and J.-M. Casagrande, "Estimation of the matrix attenuation in heterogeneous radioactive waste drums using dual-energy computed tomography," *Nucl. Inst. Meth.*, vol. A422, pp. 949–956, Feb. 1999.

[24] D. Braz, R. T. Lopes, and L. M. G. Motta, "Dual-energy computerized tomography in compacted soil," *Geotechnical Geological Eng.*, vol. 18, no. 3, pp. 221–238, 2000.

[25] O. Klein and Y. Nishina, "Über die streuung von strahlung durch freie elektronen nach der neuen relativistischen quantendynamik von dirac," *Z. Phys.*, vol. 52, pp. 853–869, 1929, (192911-12).

[26] M. L. Taylor, R. L. Smith, F. Dossing, and R. D. Franich, "Robust calculation of effective atomic numbers: The auto-zeff software," *Med. Phys.*, vol. 39, p. 1769, 2012.

[27] A. H. Compton and S. K. Allison, *X-rays in theory and experiment*. New York, NY, USA: Van Nostrand, 1935.

[28] J. S. Kallman, S. DePiero, S. Azevedo, and H. E. Martz, Jr., "Effects of powder morphology and particle size on CT number estimates," *Proc. SPIE Computational Imaging X11*, vol. 9020, p. 90200K, Mar. 2014.

[29] D. E. Cullen, J. H. Hubbell, and L. Kissel, EPDL97: The evaluated photon data library '97 version, LLNL Tech. Rep., UCRL-ID-50400, Sep. 1997, vol. 6, rev. 5.

[30] K. C. Bond, J. A. Smith, J. N. Treuer, S. Azevedo, J. S. Kallman, and H. E. Martz, Jr., ZeCalc Algorithm Details, Version 6, LLNL Tech. Rep., LLNL-TR-609327, Jan. 2013, To request a copy of ZeCalc software, contact Mary Holden-Sanchez at holdensanchez2@llnl.gov.

[31] A. K. Jain, *Fundamentals of Digital Image Processing*. Englewood Cliffs, NJ, USA: Prentice-Hall, 1989.

[32] T. Goorley, M. James, T. Booth, F. Brown, J. Bull, L. J. Cox, J. Durkee, J. Elson, M. Fensin, R. A. Forster, J. Hendricks, H. G. Hughes, R. Johns, B. Kiedrowski, R. Martz, S. Mashnik, G. McKinney, D. Pelowitz, R. Prael, J. Sweezy, L. Waters, T. Wilcox, and T. Zukaitis, "Features of MCNP6," presented at the J. Int. Conf. Supercomputing in Nuclear Applications and Monte Carlo, Paris, France, Oct. 2013.

[33] A. L. Finkelshtein and T. O. Pavlova, "Calculation of x-ray tube spectral distributions," *X-Ray Spectrom.*, vol. 28, no. 1, pp. 27–32, 1999.

[34] G. G. Poludniowski and P. M. Evans, "Calculation of x-ray spectra emerging from an x-ray tube. Part I. electron penetration characteristics in x-ray targets," *Med. Phys.*, vol. 34, no. 6, pp. 2164–74, Jun. 2007.

[35] L. Grodzins, "Optimum energies for x-ray transmission tomography of small samples," *Nucl. Instrum. Meth.*, vol. 206, pp. 541–545, 1983.

[36] J. A. Smith, D. Schneberk, J. S. Kallman, and H. E. Martz, Jr., Documentation of the LLNL and Tyndall Micro-Computed Tomography System, LLNL Tech. Rep., LLNL-TR-421377, Dec. 2009.

[37] W. T. White, III, J. A. Smith, and K. E. Morales, MicroCT: Acquisition of CT Imaging Data for Home Made Explosive Material, LLNL Tech. Rep., LLNL-TM-507819, Oct. 2011.

[38] I. M. Seetho, W. D. Brown, J. S. Kallman, H. E. Martz, Jr., and W. T. White, MicroCT: Automated Analysis of CT Reconstructed Data of Home Made Explosive Materials Using the Matlab MicroCT Analysis GUI, LLNL Tech. Rep., LLNL-TR-503291, Oct. 2011.

[39] W. D. Brown and J. A. Smith, Test Plan 75: MicroCT Test Bed Data Acquisition for Multi-Energy Zeff and Rho-e Decomposition Analysis, LLNL Tech. Rep., LLNL-TR-615552, Jan 2013, Version 3.0.

[40] M. Kass, A. Witkin, and D. Terzopoulos, "Snakes: Acltive contour models," *Intl. J. Computer Vision*, pp. 321–331, 1988.

[41] T. Heimann, V. Ginneken, M. A. Styney, Y. Arzhaeva, V. Aurich, C. Bauer, A. Beck, C. Becker, R. Beichel, G. Bekes, F. Bello, G. Binnig, H. Bischof, A. Bornik, P. M. M. Cashmann, Y. Chi, A. Cordova, B. M. Dawant, M. Fidrich, J. D. Furst, D. Fukurawa, L. Grenacher, J. Hornegger, D. Kainmuller, R. I. Kitney, H. Kobatake, H. Lamecker, T. Lange, J. Lee, B. Lennon, R. Li, S. Li, H. P. Meinzer, G. Nemeth, D. S. Raicu, A. M. Rau, E. M. van Rikxoort, M. Rousson, L. Rusko, K. A. Saddi, G. Schmidt, D. Seghers, A. Shimizu, P. Slagmolen, E. Sorantin, G. Soza, R. Susomboon, J. M. Waite, A. Wimmer, and I. Wolf, "Comparison and evaluation of methods for liver segmentation from CT datasets," *IEEE Trans. Med. Imag.*, vol. 28, no. 8, pp. 1251–1265, 2009.